Few-photon computed x-ray imaging

Zheyuan Zhu[1, a)] and Shuo Pang[1]
[1]CREOL, The College of Optics and Photonics
4304 Scorpius St. Orlando, FL, 32816, USA

X-ray is a ubiquitous imaging modality in clinical diagnostics and industrial inspections, thanks to its high penetration power. Conventional transmission-based x-ray radiography or computed tomography (CT) systems collect approximately $10^3 - 10^4$ counts per pixel to ensure sufficient signal to noise ratio (SNR). Recent development of energy sensitive photon counting detectors has made x-ray imaging at low photon flux possible. In this paper, we report a photon-counting scheme that records the time stamp of individual photons, which follows a negative binomial distribution, and demonstrate the reconstruction based on the few-photon statistics. The x-ray projection and tomography reconstruction from measurements of ~16 photons per beam show the potential of using photon counting detectors for dose-efficient x-ray imaging applications.

Keywords: Photon statistics, Photon counting, Computed tomography

Due to its high penetrating power, x-ray imaging is extensively used as a non-invasive imaging method in medical diagnosis and industrial inspections. X-ray imaging modalities based on attenuation is the most common mechanism of radiography (projection) and computed tomography (CT). Conventional transmission-based x-ray imaging systems count $10^3 - 10^4$ photons per pixel in a fixed period[1]. To ensure the signal-to-noise ratio (SNR) on the detector, high radiation dose is administrated to the sample[2], prohibiting the imaging of objects that are susceptible to radiation damage. Conformational change due to high radiation dose is a major concern for imaging of biological samples[3,4]. Microprocessors and flash memories are also vulnerable to physical damages under excessive x-ray radiation[5,6]. Phase retrieval techniques have been developed to alleviate the measurement noise and recover the complex refractive index from low-dose measurements[7], yet the demand for coherent X-ray source challenges its adoption in practical applications[8]. Developing a table-top, transmission-based x-ray imaging system at extremely low photon flux is highly desirable for biomedical diagnosis and industrial inspection[9,10].

In visible and infrared optical imaging regime, the use of avalanche photodiodes to time-resolve the single-photon events allows the range and reflectivity imaging at a few photons per pixel[11,12]. X-ray detector with single-photon sensitivity has opened up opportunities for photon-efficient imaging in medical CT and integrated circuit inspections[13,14]. The current usage of x-ray photon-counting detectors is limited to the traditional time-integration mode, which counts the total number of photons in a predefined integration time. Here we report a photon-counting scheme that records the time stamp of individual x-ray photons, which follows a negative binomial distribution. We have demonstrated the reconstruction under low photon flux by taking the few-photon statistics into consideration.

Instead of collecting the total number of photon per pixel, our photon-counting method records the number of time intervals elapsed until a predefined number of photons are received. Fig. 1 shows the concept of operation. The time

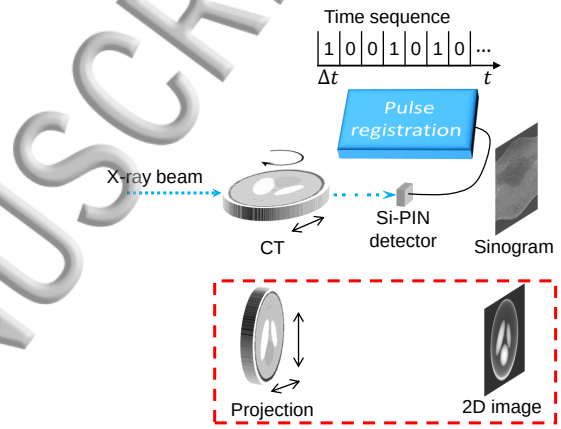

FIG. 1. Illustration of the photon-counting scheme for both x-ray projection and tomography imaging.

stamps of individual photons collected from the Si-PIN detector are registered by a data-acquisition device. Let λ be the probability of receiving one photon in each time interval, Δt, when no sample is present. In experiment, λ is the product between source flux and detector quantum efficiency. Considering the sample attenuation, for each pencil beam, j, the probability of receiving one photon in each time interval is

$$T_j = \lambda \exp(-\sum_{i=1}^{n} \mathbf{A}_{ij}\mathbf{f}_i) \tag{1}$$

where the subscript $i = 1,2,...,n$ represents the index of the discretized object attenuation map $\mathbf{f}$; and $j = 1,2,...,m$ represents the index of discretized pencil-beam measurements. The matrix A establishes the linear relation between the object and the measurement. For x-ray projection imaging, $\mathbf{A}$ is the identity matrix, and for tomography, $\mathbf{A}$ represents the Radon transform matrix constructed from the distance-driven ray-tracing model[15].

The joint probability of detecting the $\mathbf{r}$-th photon at $\mathbf{g}$-th time interval follows the negative binomial distribution $\mathbf{g} \sim NB(\mathbf{r},\mathbf{T})$ $(\mathbf{r} \in \mathbb{N}_+^m, \mathbf{g} \in \mathbb{N}_+^m)$, whose probability mass function

[a)]Electronic mail: zyzhu@knights.ucf.edu

This manuscript was accepted by Appl. Phys. Lett. Click here to see the version of record.

(PMF) is

$$p(\mathbf{g}|\mathbf{f};\mathbf{r}) = \prod_{j=1}^{m} \binom{g_j - 1}{r_j - 1} (1-T_j)^{g_j - r_j} (T_j)^{r_j} \quad (2)$$

where $\mathbf{g} = (g_1, g_2, ..., g_m)$ is the total number of time intervals that has elapsed upon the arrival of the first $\mathbf{r} = (r_1, r_2, ..., r_m)$ photons at each pencil beam, j. In Eq.1 and 2, if we set $\mathbf{r}$ to 1 and $\mathbf{A}$ to identity matrix, the resulting PMF will have the same form as that of the single-photon reflectivity imaging in Ref. 11. Conventional time-integration photon-counting scheme records the number of photons detected in a predefined period $\mathbf{g}\Delta t$, during which the joint probability of receiving $\mathbf{r}$ photons for each pencil beam follows binomial distributed $\mathbf{r} \sim B(\mathbf{g}, \mathbf{T})$ ($\mathbf{g} \in \mathbb{N}_+^m, \mathbf{r} \in \mathbb{N}^m$)

$$p(\mathbf{r}|\mathbf{f};\mathbf{g}) = \prod_{j=1}^{m} \binom{g_j}{r_j} (1-T_j)^{g_j - r_j} (T_j)^{r_j} \quad (3)$$

Notice that if T_j is small ($T_j < 0.01$) and g_j is sufficiently large ($g_j > 100$), Eq.3 can be approximated by a Poisson distribution $r_j \sim \text{Poisson}(g_j T_j)$. The reconstruction from the photon-counting measurement follows the maximum-a-posteriori (MAP) framework, which maximizes the posterior likelihood of $\mathbf{f}$ under the total-variance (TV) prior $\pi(\mathbf{f}) = \exp(-\tau TV(\mathbf{f}))$, where $TV(\mathbf{f})$ denotes the TV regularizer[16]. Here we introduce negative logarithm to the posterior distribution in the MAP framework:

$$\hat{\mathbf{f}} = \text{argmin}_{\mathbf{f}'} \{ l(\mathbf{f}') + \tau TV(\mathbf{f}') \} \quad (4)$$

where the objective function consists of two parts after neglecting terms independent on $\mathbf{f}$: the first part is the negative log-likelihood, $l(\mathbf{f}) = -\log(p(\mathbf{g}|\mathbf{f};\mathbf{r}))$ for negative binomial distribution, and $l(\mathbf{f}) = -\log(p(\mathbf{r}|\mathbf{f};\mathbf{g}))$ for binomial distribution; the second part $TV(\mathbf{f})$ is a TV regularizer with a non-negative parameter τ. Both the conventional and our time-stamp photon counting schemes have the same negative log-likelihood

$$l(\mathbf{f}) = \sum_{j=1}^{m} [r_j \sum_{i=1}^{n} \mathbf{A}_{ij} \mathbf{f}_i - (g_j - r_j) \log(1 - T_j)] \quad (5)$$

with gradient

$$\nabla l(\mathbf{f}) = \mathbf{A}^T [r - \frac{\lambda (g-r) \exp(-\mathbf{A}\mathbf{f})}{1 - \lambda \exp(-Af)}] \quad (6)$$

and Hessian matrix

$$\mathbf{H}(l(\mathbf{f})) = \mathbf{A}^T (\frac{\lambda (g-r) \exp(-\mathbf{A}\mathbf{f})}{(1 - \lambda \exp(-\mathbf{A}\mathbf{f}))^2}) \mathbf{A} \quad (7)$$

The MAP problem in Eq.4 is solved with a customized SPIRAL-TAP algorithm[17] based on the gradient and Hessian of the likelihood functions. The algorithm terminates when the relative change in the objective function between two consecutive iterations is smaller than 10^{-6}. To prevent over-smoothing the image, we enumerated various TV regularization parameters, τ, and selected the one that yielded minimal objective function at the end of the iterations.

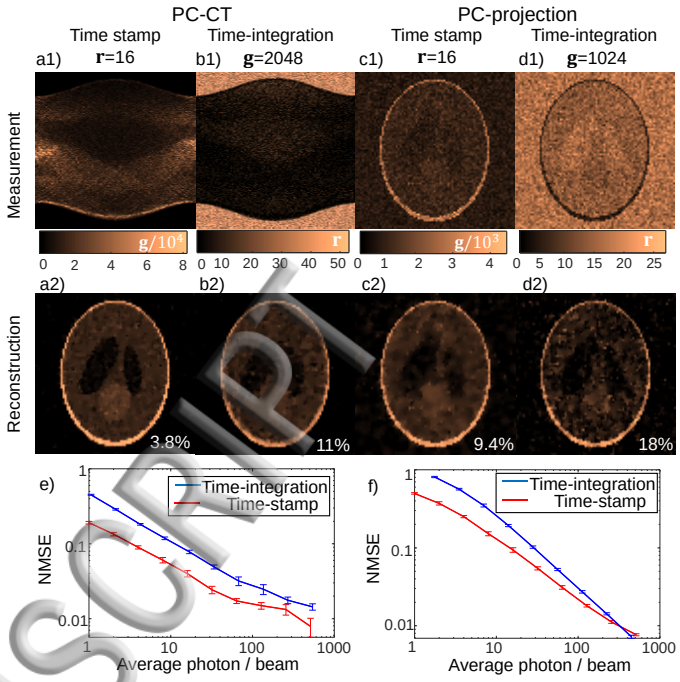

FIG. 2. PC-CT and PC-projection simulation and reconstruction of the Shepp-Logan phantom under different photon-counting schemes. (a1) time-stamp PC-CT measurement; (b1) time-integration PC-CT measurement; (c1) time-stamp PC-projection measurement; (d1) time-integration PC-projection measurement. (a2-d2) reconstruction from (a1-d1), respectively. The numbers on each sub-figure indicate the NMSE between reconstruction and ground truth. (e, f) Log-scale plot of the reconstruction NMSE vs. the photon counts per beam for (e) PC-CT and (f) PC-radiography. All error bars indicate the variance within 10 simulation instances.

We first performed a simulation on the conventional time-integration and our time-stamp photon-counting schemes applied to both x-ray projection (PC-projection) and CT (PC-CT) scenarios. The simulation Shepp-Logan phantom was a 16mm by 16mm 2D layer sampled at a voxel size of 0.2 mm^3. PC-projection was simulated with a pixel-wise measurement. PC-CT was simulated with 0.2mm translation step size and 90 projections uniformly sampled in 0 180°. For conventional time-integration scheme (Fig. 2(a, c)), each simulation instance generates binomial random numbers $\mathbf{r}$ in $\mathbf{g}$ time intervals. For time-stamp photon-counting scheme (Fig. 2(b, d)), the measurement, $\mathbf{g}$, is a sum of $\mathbf{r}$ geometric random numbers to represent the time intervals before the arrival of the $\mathbf{r}$-th photon. Fig. 2(a, b) show the time-integration and time-stamp PC-CT with comparable average photon count per pencil beam. The measurement for time-integration PC-CT (Fig. 2(a)) was simulated with $\mathbf{g}$=2048 time intervals (average 16.9 photons / beam), while time-stamp PC-CT (Fig. 2(b)) only counts the elapsed time intervals of the first $\mathbf{r}$=16 photons. Fig. 2(e) plots the log-scale normalized mean square error NMSE $= \|\hat{\mathbf{f}} - \mathbf{f}_0\|^2 / \|\mathbf{f}_0\|^2$ versus the average number of photons per pencil beam. The error bars indicate the variance of NMSE arising from 10 simulation instances. Fig. 2(c, d) compare the time-integration ($\mathbf{g} = 1024$ intervals, average

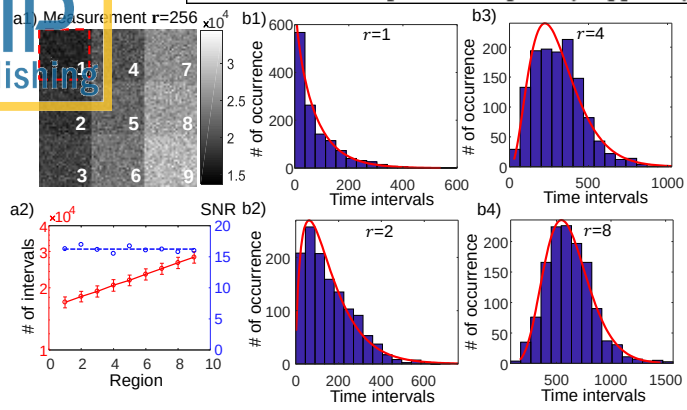

FIG. 3. Experimental observation of the photon-counting noise model. (a1) Number of time intervals before the arrival of 256th photon. (a2) Time intervals in each region. Red dots and error bars represent the mean and standard deviation. Blue does represent the SNR. (b1-b4) Histograms of the number of time intervals elapsed before r=1, 2, 4, and 8 photons are detected in region 1.

15.6 photons / beam) and time-stamp PC-projection (**r**=16 photons / beam). The weakly contrasted features within the skull of the phantom are hardly visible at low photon counts, which agrees with the previous experiment result[18]. The reconstruction NMSE versus average photon count is plotted in Fig. 2(f). Fig. 2(e, f) shows that in the low photon-counting regime ($\mathbf{r} < 100$) of both PC-projection and PC-CT, the reconstruction NMSE of the conventional time-integration scheme is higher than our time-stamp scheme. This is mainly attributed to the low photon counts, and thus poor SNR in the high-attenuation or thick regions when measured with a predefined integration time. In contrast, our proposed time-stamp scheme adaptively changes the wait time of each pencil beam until a predefined number of photons are detected, thus guaranteeing relatively uniform SNR regardless of the sample attenuation or thickness. Comparing Fig. 2(e) and (f), it is worth noticing that PC-CT generally has a smaller NMSE than PC-projection because CT absorbs more incident radiation along the beam for the same number of detected photons.

The photon-counting projection and tomography experiments used a filtered copper-anode x-ray source (XRT60, Proto Manufacturing) operating at 12kV, 1mA. This low power setting avoided the overlap of two photon incidences within one time interval when no sample was present. The x-ray beam was collimated by a pair of 0.5mm pinholes, placed 180mm downstream the x-ray focus, to form a pencil-beam illumination. This created a beam spot size of 0.6mm on the sample plane, which was located 300mm from the x-ray focus. Notice that the spatial blurring arising from multiple scatterings among adjacent voxels is insignificant because the area of the detector is small, and the scattering cross-section is one order of magnitude smaller than the absorption cross-section for the energy used in our experiments[19]. A Si-PIN detector (X-123, AMPTEK) was connected to a data-acquisition (DAQ) device (USB-6353, National Instrument) programmed in the edge-counting mode. To eliminate dark noise, the low-energy channels (<1keV) on the detector were filtered out by the detector's built-in pulse-height discrimination. In data acquisition, only the time stamps of photons whose energy falls within 10 ± 0.5keV were recorded. The output of the DAQ device was a series of Δt=10s time intervals, within which either one photon or zero photon was registered. In PC-projection, the sample was translated both horizontally and vertically across the beam by two linear stages (UTM150CC, Newport). In PC-CT the sample was also rotated 180° around the vertical axis by a rotational stage (RV1200P, Newport). A laser-machined acrylic resolution target and a slice of mouse brain sample were used to evaluate the performance of PC-CT. The resolution target consists of groups with 0.5mm to 1.0mm line-width at 0.1mm interval. The size of the mouse brain sample was 10mm X 6mm after air-drying to prevent deformation during the scan. Both objects were scanned at a step size of 0.1mm in the transverse dimension, and 1° in the rotation dimension to cover 180° projections. To facilitate the data analysis, we acquired a complete time stamp within 1s for both objects. The net imaging time for detecting 16 photons was 17 minutes for the resolution target, 5 minutes for the mouse brain. In practice, the mechanical movement and detector synchronization took extra time. Notice than parallel acquisition using photon-counting detector array with higher counting rate ($10^{8\sim10}$ counts/second) could reduce the net imaging time to $\sim$ 1 minute. For comparison with flat panel detector (FPD), we also performed a CT scan on the mouse brain sample with a scintillator-based detector (1215CF-MP, Rayence). The source-side collimators were removed to directly capture each cone-beam projection. The source current was increased to 40mA to overcome the dark noise on the FPD. The FPD was triggered continuously at 10 frames per second, and the first several frames (between 1 to 30 frames) were summed up to obtain images at different integration time settings (ranging from 0.1s to 3s), each corresponding to a different readout intensity level.

The noise model of our photon-counting system and the incident photon flux λ were calibrated with a projection measurement on a linear attenuation pattern, which was created by stacking multiple paper layers with identical thickness h=0.12mm. The pattern was divided in to 3 X 3 regions, with region 1 being air and region 9 corresponding to 8 paper layers. We performed a PC-projection scan (Fig. 3(a1)) covering all 9 regions of the paper pattern, and waited for the arrival of the **r**=256th photon at each point. Fig. 3(a2) plots the average and standard deviation of the time intervals, **g**, within each region in log scale. The ratio between the average and standard deviation fluctuates around 16.2, suggesting that the measurement uncertainty agrees with the the shot-noise limit, the square root of photon counts. The linearity of the curve agrees with the exponential decay in the transmission as the thickness increases. From the slope in Fig. 3(a2), we estimated the transmittance, t=93% per paper layer. To directly observe the distribution of time intervals, we varied the number of photons, **r**, to collect at each point. Fig. 3(b1-b4) plot the histogram of **g** within region 1 at **r**=1, 2, 4 and 8. We fit a negative binomial model with one unknown, T, on each histogram. The red curves plot the negative binomial distributions with fitted parameter, T, which are 0.0127, 0.0128,

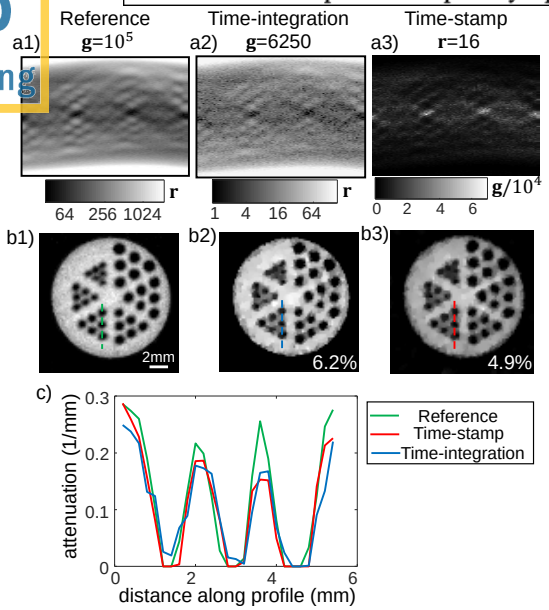

FIG. 4. Measurement (a) and reconstruction (b) of 1) reference image, 2) time-integration PC-CT scheme (17.8 photons/beam on average) and 3) time-stamp PC-CT (16 photons/beam) of a resolution target. (c) attenuation profile along the dashed line (0.7mm line-width group) in (b1-b3).

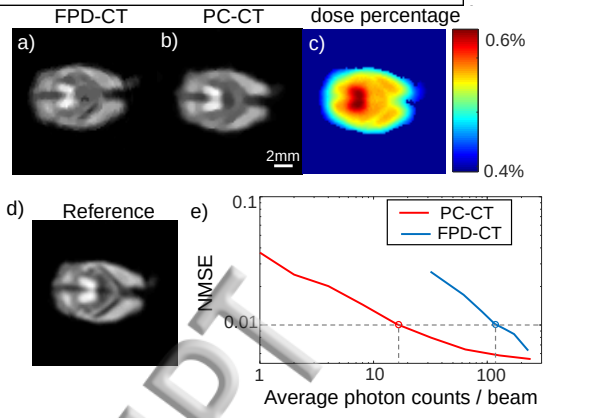

FIG. 5. Mouse brain sample imaged with (a) panel detector (FPD-CT, average 116.2 detector readout / beam) and (b) time-stamp PC-CT (16 photons / beam). (c) Radiation dose ratio between time-stamp PC-CT and FPD-CT. (d) Reference image with 1s integration time per pencil beam (e) NMSE versus average photon counts per beam for time-stamp PC-CT and panel detector.

0.0129, and 0.0129 respectively in (b1)-(b4). The high consistency signifies the same photon flux exhibited on all histograms. The incident photon flux λ was calibrated from the T in region 1.

With the calibrated incident photon flux and experimentally verified noise model, a time-stamp PC-CT scan and reconstruction were performed on the acrylic resolution target, and compared with conventional, time-integration photon-counting scheme. Fig. 4(a1) shows the number of counts **r** in the time-integration photon-counting scheme within 1s integration time ($\mathbf{g} = 10^5$). The average number of photons per beam was 569. The reconstructed image (Fig. 4(b1)) was used as reference for evaluating low-photon-count images. Fig. 4(a2) shows the measurement of time-integration PC-CT with reduced integration time (0.0625s). The photon count per pencil beam was 17.8 on average. Fig. 4(a3) displays the number of elapsed time intervals **g** before the arrival of **r**=16th photon at each beam. The reconstructed attenuation map from time-integration and time-stamp PC-CT are shown in Fig. 4(b2, b3), respectively. The intensity profile of 0.7mm group is plotted in Fig. 4(c), which shows a visibility of 0.82 on reference image, and 0.68, 0.60 for time-integration and time-stamp PC-CT, respectively. Both time-integration and time-stamp PC-CT are capable of reconstructing small details with discernible contrast at low photon flux, because x-ray photon-counting detector eliminates the dark noise via filtration on the low-energy channels. The spatial resolution is limited by the 0.6mm spot size on the sample plane due to the beam divergence. With approximately the same average photon count (Fig. 4(b2) and (b3)), time-integration and time-stamp PC-CT have normalized mean square difference of 6.2% and 4.9% with respect to the reference image. We speculate that this slight difference is primarily attributed to the more uniform SNR on the sinogram of time-stamp PC-CT.

PC-CT has the potential to reduce the radiation dose, which is especially attractive for biomedical imaging applications. We compared the image of a mouse brain layer obtained from time-stamp PC-CT and a flat panel detector (FPD-CT, for short). Fig. 5 shows the reconstruction from FPD-CT (a, 0.5s integrating time (5 frames), 116.2 detector readout per beam on average) and time-stamp PC-CT (b, 16 photons per beam). A comparison on the absorbed radiation doses between Fig. 5(a) and (b) was performed through Monte Carlo simulation. The irradiance of the source was computed using *XSPECT* under experimental power settings. The radiation dose of time-stamp PC-CT was calculated via an equivalent tube current modulation to simulate different integration time for each pencil beam with *ImpactMC*[20]. Fig. 5(c) plots the percentage of PC-CT radiation dose with respect to that in FPD-CT. The proposed time-stamp PC-CT reduces the dose to ~0.6% of FPD-CT, because the photon-counting detector eliminates the dark noise commonly found on panel detectors, and thus a much lower source flux could be used for image acquisition. Fig. 5(c) shows that the dose reduction on the surface is more prominent than the interior region. This is because the transmission signal from the interior region is weaker, and the time-stamp scheme would wait for a longer time until the predefined photon counts are received.

To further evaluate the performance between time-stamp PC-CT and FPD-CT, we acquired a complete photon time stamp spanning 1s integration time (1283 photon counts per beam on average) for the mouse brain sample, and reconstructed a reference image (Fig. 5(d)) from all the detected photons. Fig. 5(e) plots the normalized mean square difference between the reconstruction and the reference in log scale. The blue and red circles on the plot correspond to FPD-CT

and time-stamp PC-CT in Fig. 5(a) and (b), respectively. For low photon counts, time-stamp PC-CT consistently performs better than conventional CT. As the photon count increases, panel detector eventually will have a comparable reconstruction error as that of time-stamp PC-CT. This is because, in high-photon flux regime, the noise model of using the panel detector and photon counting module can both be approximated by a Gaussian distribution.

In summary, we have demonstrated an x-ray photon-counting imaging scheme tailored to low photon flux scenarios. The presented method records the arrival time stamp of individual photons and reconstructs the image with a few photons per pixel, which is applicable to both x-ray projection and CT. Our photon statistics model agrees with the actual time stamp of detected photons in the experiment. We are able to reconstruct the PC-CT image from the arrival time stamp of the first 16 photons using a customized SPIRAL-TAP algorithm based on the negative binomial likelihood. In contrast to the conventional photon-counting scheme that records the total number of photons in a predefined integration time, our time-stamp photon-counting scheme adaptively chooses the wait time to maintain the same number of detected photons for each beam. This ensures uniform SNR across all measurements, especially for high-attenuation or interior regions on CT sinogram. The proposed few-photon method reduces the radiation dose by 2 orders of magnitude compared to CT using a panel detector. Our PC-CT scheme could be extended to cone-beam. We envision the photon-counting detector array can be applied in tandem with a location addressable illumination mask, which can provide modulation to the cone beam illumination. The reduced dose opens up opportunities in dose-sensitive biomedical or industrial non-invasive inspection applications. In addition to the presented projection and CT modalities, the photon-counting scheme can also be applied to reduce the imaging time of x-ray diffraction tomography[21], where the diffraction signal is intrinsically 3 orders of magnitude weaker than the transmitted signal[22]. We could further exploit the energy sensitivity of X-ray photon-counting detectors to perform energy-dispersive CT or diffraction tomography for three-dimensional material identification.

[1] P. M. Shikhaliev, T. Xu, and S. Molloi, "Photon counting computed tomography: concept and initial results," Medical physics **32**, 427–436 (2005).

[2] P. Villanueva-Perez, S. Bajt, and H. N. Chapman, "Dose efficient compton x-ray microscopy," Optica **5**, 450 (2018).

[3] M. Weik, R. B. G. Ravelli, G. Kryger, S. McSweeney, M. L. Raves, M. Harel, P. Gros, I. Silman, J. Kroon, and J. L. Sussman, "Specific chemical and structural damage to proteins produced by synchrotron radiation," Proceedings of the National Academy of Sciences **97**, 623–628 (2000).

[4] R. B. Ravelli and S. M. McSweeney, "The 'fingerprint' that x-rays can leave on structures," Structure **8**, 315–328 (2000).

[5] D. Bernard and R. Blish, "Considerations for minimizing radiation doses to components during x-ray inspection," in *2005 7th Electronic Packaging Technology Conference* (IEEE, 2005).

[6] A. Ditali, M. Ma, and M. Johnston, "X-ray inspection-induced latent damage in DRAM," in *2006 IEEE International Reliability Physics Symposium Proceedings* (IEEE, 2006).

[7] M. J. Kitchen, G. A. Buckley, T. E. Gureyev, M. J. Wallace, N. Andres-Thio, K. Uesugi, N. Yagi, and S. B. Hooper, "Ct dose reduction factors in the thousands using x-ray phase contrast," Scientific reports **7**, 15953 (2017).

[8] A. Bravin, P. Coan, and P. Suortti, "X-ray phase-contrast imaging: from pre-clinical applications towards clinics," Physics in Medicine & Biology **58**, R1 (2012).

[9] A.-X. Zhang, Y.-H. He, L.-A. Wu, L.-M. Chen, and B.-B. Wang, "Tabletop x-ray ghost imaging with ultra-low radiation," Optica **5**, 374 (2018).

[10] X. Huang, H. Miao, J. Steinbrener, J. Nelson, D. Shapiro, A. Stewart, J. Turner, and C. Jacobsen, "Signal-to-noise and radiation exposure considerations in conventional and diffraction x-ray microscopy," Optics Express **17**, 13541 (2009).

[11] A. Kirmani, D. Venkatraman, D. Shin, A. Colaço, F. N. C. Wong, J. H. Shapiro, and V. K. Goyal, "First-photon imaging," Science **343**, 58–61 (2013).

[12] A. McCarthy, N. J. Krichel, N. R. Gemmell, X. Ren, M. G. Tanner, S. N. Dorenbos, V. Zwiller, R. H. Hadfield, and G. S. Buller, "Kilometer-range, high resolution depth imaging via 1560 nm wavelength single-photon detection," Optics Express **21**, 8904 (2013).

[13] K. Taguchi and J. S. Iwanczyk, "Vision 20/20: Single photon counting x-ray detectors in medical imaging," Medical Physics **40**, 100901 (2013).

[14] A. Markman and B. Javidi, "Integrated circuit authentication using photon-limited x-ray microscopy," Optics Letters **41**, 3297 (2016).

[15] R. L. Siddon, "Fast calculation of the exact radiological path for a three-dimensional CT array," Medical Physics **12**, 252–255 (1985).

[16] A. Beck and M. Teboulle, "Fast gradient-based algorithms for constrained total variation image denoising and deblurring problems," IEEE Transactions on Image Processing **18**, 2419–2434 (2009).

[17] Z. T. Harmany, R. F. Marcia, and R. M. Willett, "This is SPIRAL-TAP: Sparse poisson intensity reconstruction ALgorithms—theory and practice," IEEE Transactions on Image Processing **21**, 1084–1096 (2012).

[18] K. M. Sowa, B. R. Jany, and P. Korecki, "Multipoint-projection x-ray microscopy," Optica **5**, 577 (2018).

[19] M. Berger, "Xcom: photon cross sections database," http://www.nist.gov/pml/data/xcom/index.cfm (2010).

[20] W. Chen, D. Kolditz, M. Beister, R. Bohle, and W. A. Kalender, "Fast on-site monte carlo tool for dose calculations in CT applications," Medical Physics **39**, 2985–2996 (2012).

[21] Z. Zhu, A. Katsevich, A. J. Kapadia, J. A. Greenberg, and S. Pang, "X-ray diffraction tomography with limited projection information," Scientific Reports **8** (2018), 10.1038/s41598-017-19089-w.

[22] S. Pang, Z. Zhu, G. Wang, and W. Cong, "Small-angle scatter tomography with a photon-counting detector array," Physics in Medicine and Biology **61**, 3734–3748 (2016).

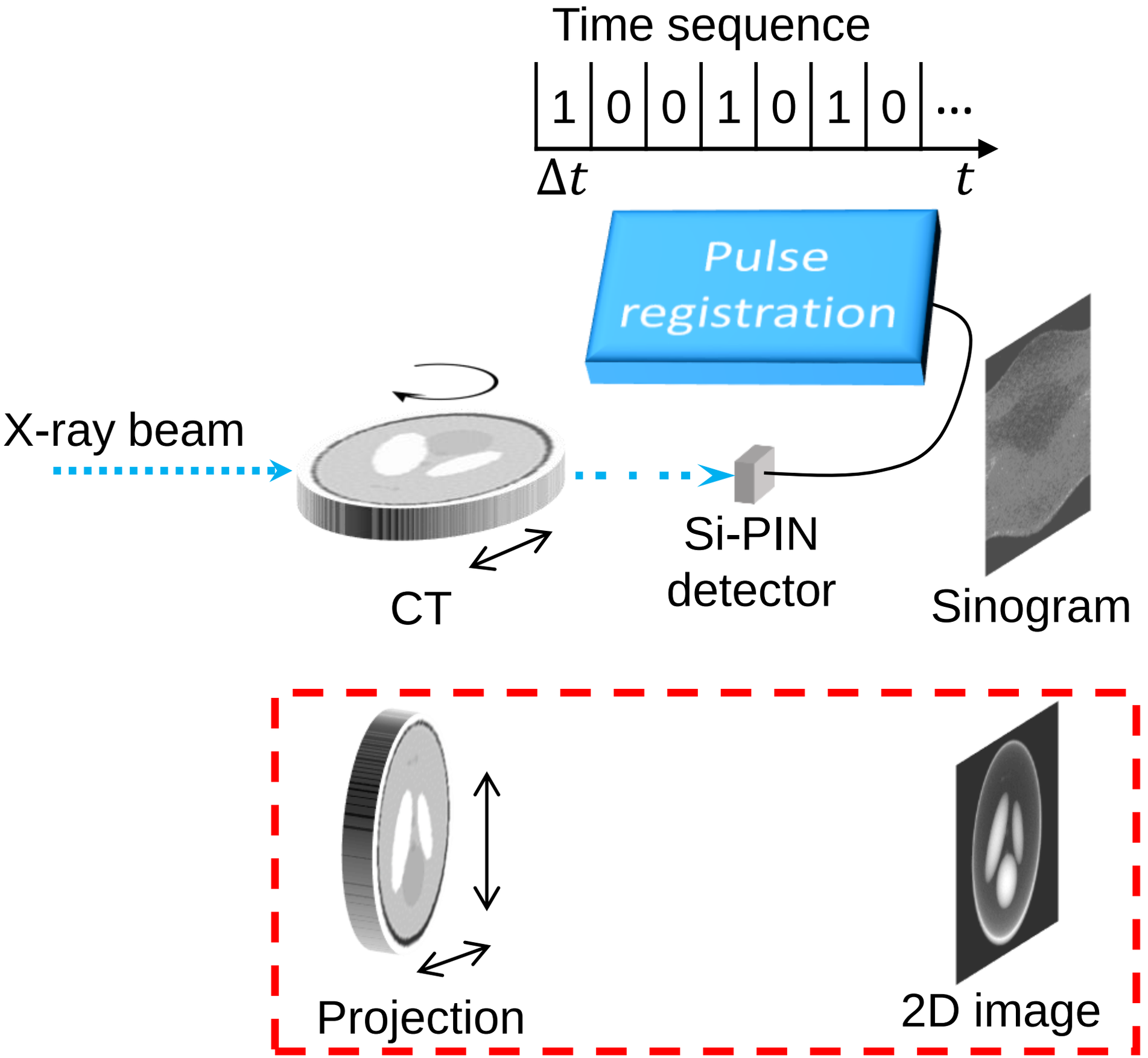
Time sequence
1 0 0 1 0 1 0 ...
Δt
t
Pulse registration
X-ray beam
CT
Si-PIN detector
Sinogram
Projection
2D image

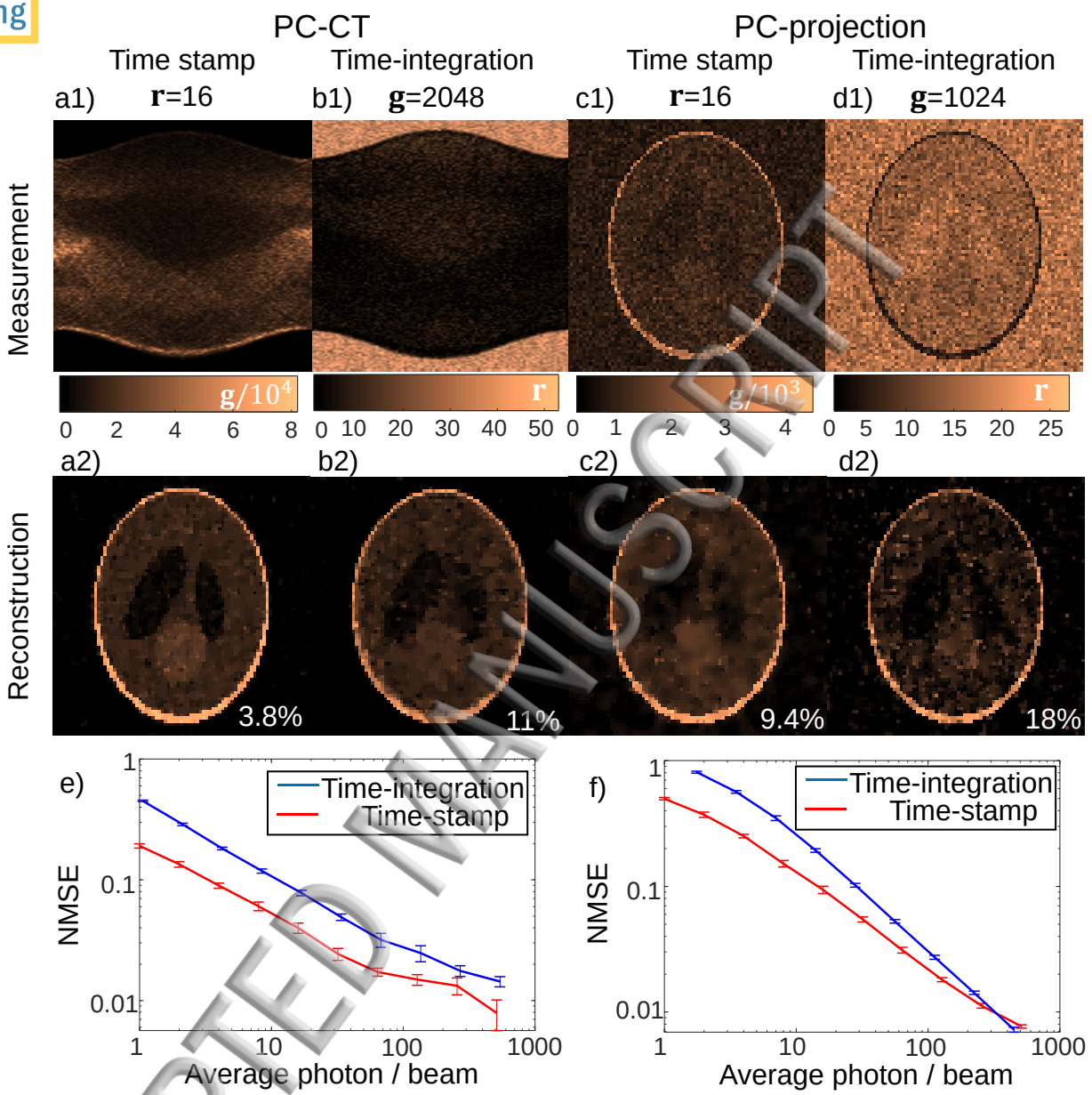

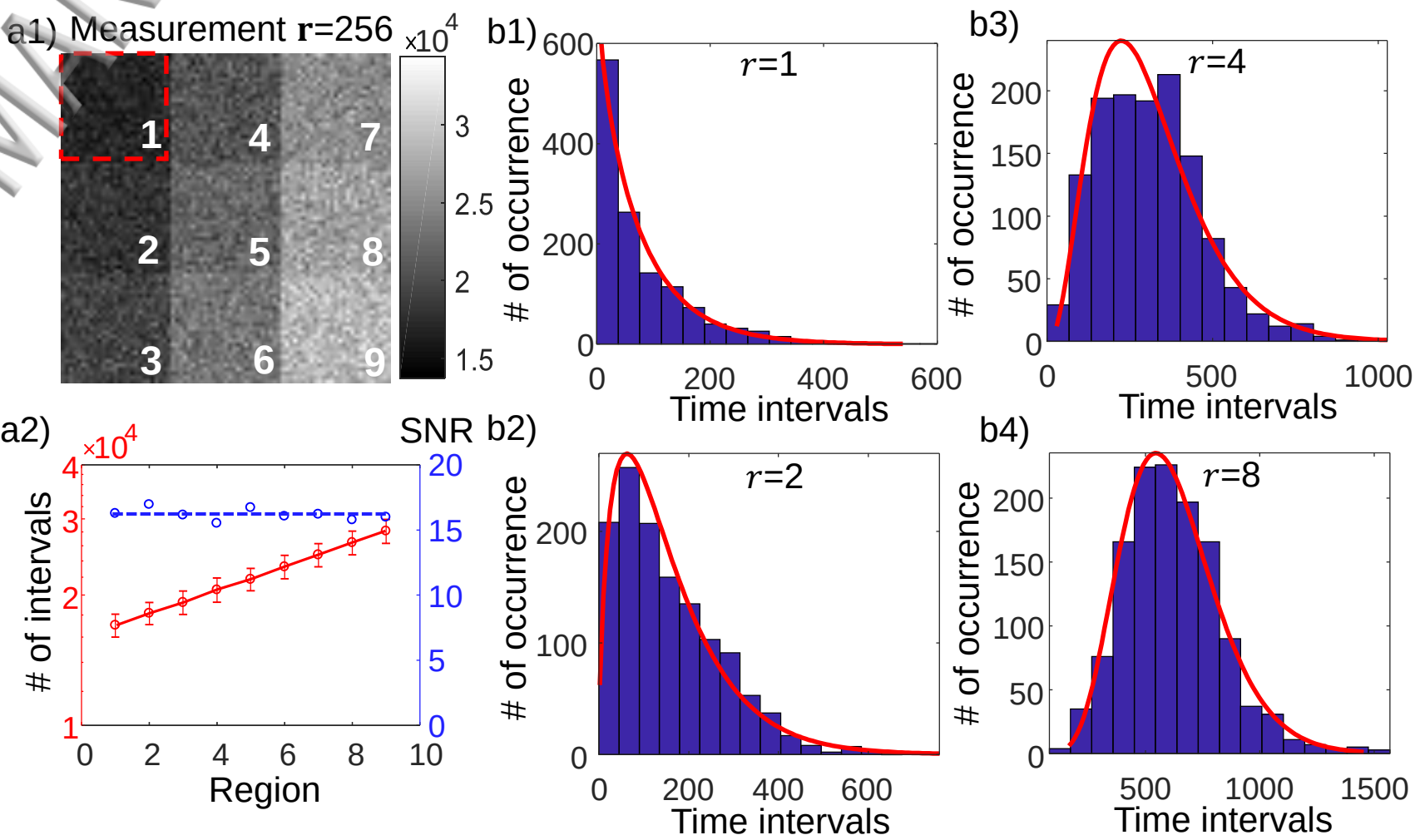
a1) Measurement r=256
×10^4
3
2.5
2
1.5
1
2
3
4
5
6
7
8
9
b1)
r=1
# of occurrence
Time intervals
b3)
r=4
# of occurrence
Time intervals
a2)
SNR
×10^4
# of intervals
Region
b2)
r=2
# of occurrence
Time intervals
b4)
r=8
# of occurrence
Time intervals

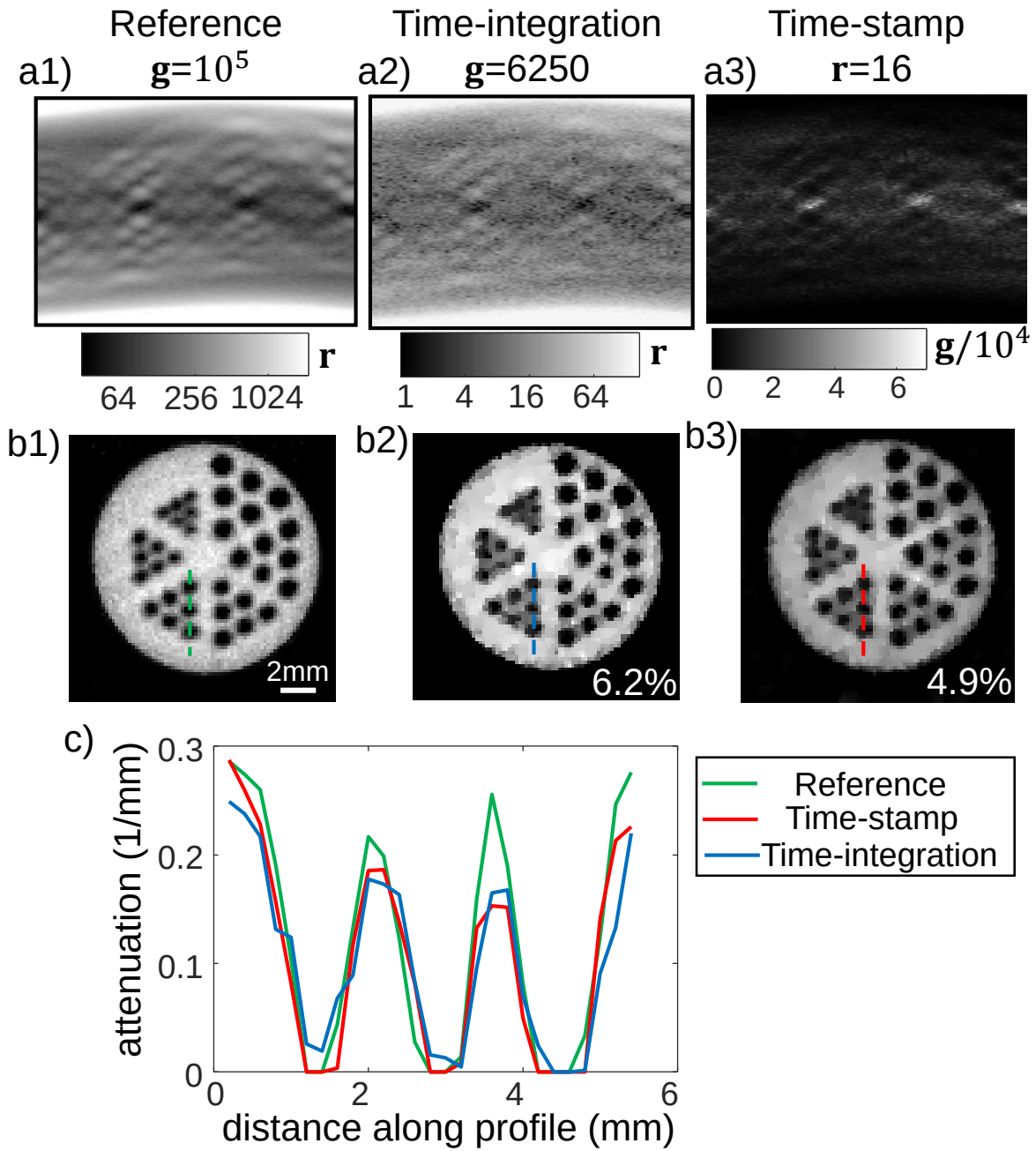
Reference
Time-integration
Time-stamp
a1)
g=10^5
a2)
g=6250
a3)
r=16
r
64 256 1024
r
1 4 16 64
g/10^4
0 2 4 6
b1)
b2)
b3)
2mm
6.2%
4.9%
c)
attenuation (1/mm)
0.3
0.2
0.1
0
0 2 4 6
distance along profile (mm)
Reference
Time-stamp
Time-integration

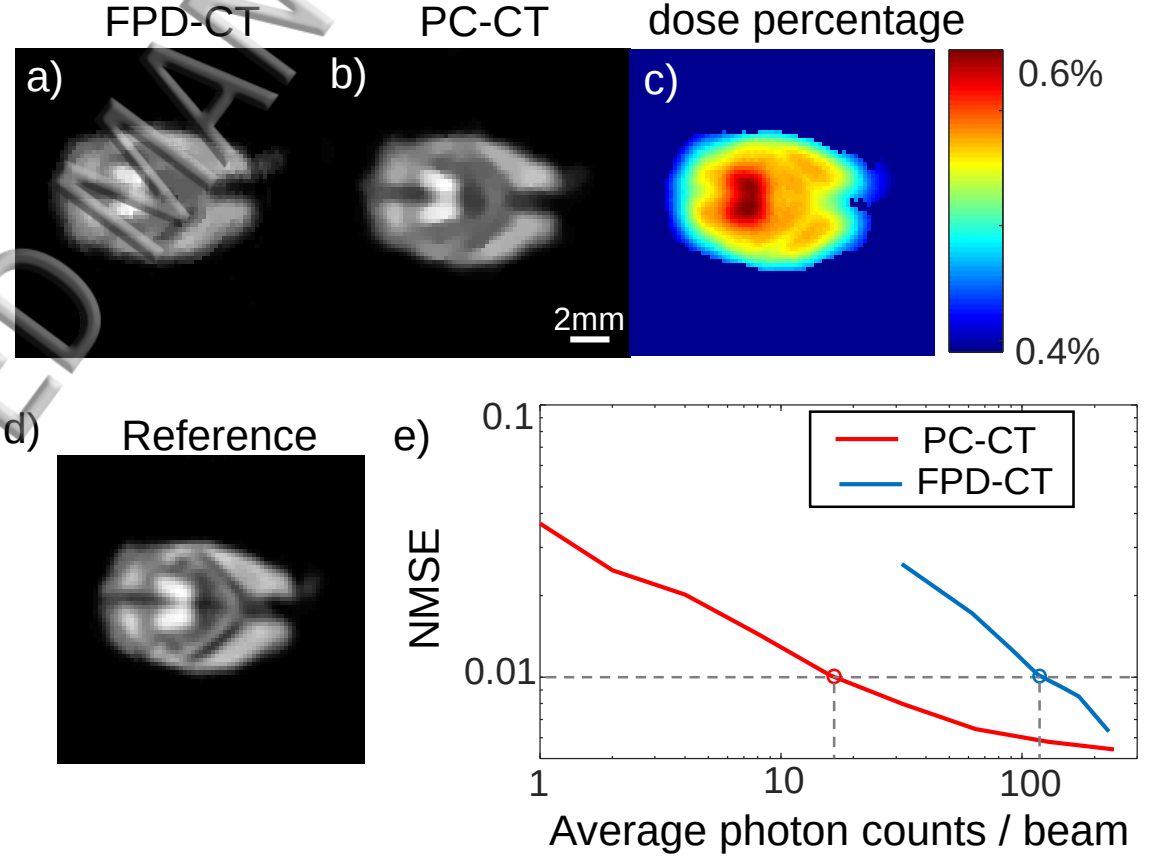
FPD-CT
PC-CT
dose percentage
a)
b)
c)
0.6%
0.4%
2mm
d)
Reference
e)
0.1
0.01
NMSE
PC-CT
FPD-CT
1
10
100
Average photon counts / beam